Investigation of Surface Nanostructuring, Mechanical Performance and Deformation Mechanisms of AISI 316L Stainless Steel Treated by Surface Mechanical Impact Treatment

Milad Rostami[1] · Reza Miresmaeili[1] · Asghar Heydari Astaraee[2]

Abstract

Nanostructured materials exhibit superior properties with respect to their bulk counterpart. Recently, a new processing method for surface nanostructuring of metallic materials called surface mechanical impact treatment (SMIT) was developed. In this study, the surface microstructural features due to the refinement process of AISI 316L stainless steel by means of SMIT and subsequent mechanical performance were investigated. The effects of SMIT processing parameters, i.e. ball size and treatment duration, were studied in terms of microstructural evolutions using X-ray diffraction, transmission electron microscopy, optical microscopy, and field emission scanning electron microscopy analyses, and mechanical properties through hardness and tensile tests. A gradient nanostructured surface layer was successfully formed on the surface of the treated samples. The mean grain size was measured to be ~ 20 nm in the topmost surface layer and increased with increasing depth. Microstructural examinations showed that the twins and their intersections (rhombic blocks) formed in the surface layers. It was found that the mechanical performance of the treated samples is effectively enhanced. The surface hardness of the treated samples increased about 3 times while the yield strength of the samples increased with increasing SMIT time and size of the ball up to 2.5 times. The grain refinement mechanisms, mechanical properties, and fracture behavior were subsequently analyzed and discussed.

List of Symbols

Latin Script Symbols

A	Zener anisotropy
b	Burgers vector
C	Elastic stiffness coefficient
D	Grain size
d	Diameter of the ball
G	Shear modulus
I	Intensity
$K_{111}\omega_0$	Proportionality constant
$f_{\alpha'}$	Volume fraction of α'-martensite
R	Reliability factor
t	Time

Greek Script Symbols

α	Stacking fault probability
α_0	Unit cell edge dimension
γ	Stacking fault energy
ρ	Dislocation density
ε	Lattice microstrain

Abbreviations

AISI	American Iron and Steel Institute
DIM	Deformation induced martensite
FESEM	Field emission scanning electron microscopy
FCC	Face centered cubic
HCP	Hexagonal closest packed
OM	Optical microscopy
SAED	Selected area electron diffraction
SF	Stacking fault
SFE	Stacking fault energy
SFP	Stacking fault probability

✉ Reza Miresmaeili
miresmaeili@modares.ac.ir

1   Department of Materials Engineering, Tarbiat Modares University, P.O. Box, Tehran 14115-143, Iran

2   Department of Mechanical Engineering, Politecnico Di Milano, 20156 Milan, Italy

SFT   Stacking fault tetrahedra
SMAT   Surface mechanical attrition treatment
SMGT   Surface mechanical grinding treatment
SMIT   Surface mechanical impact treatment
SMRT   Surface mechanical rolling treatment
SPD   Severe plastic deformation
TEM   Transmission electron microscopy
TRIP   Transformation induced plasticity
UIP   Ultrasonic impact peening
UIT   Ultrasonic impact treatment
XRD   X-ray diffraction

1 Introduction

Considering the decisive role of the surface in the functioning of materials and the life endurance of engineering components, one of the most significant and widely explored areas is the microstructural alteration of metallic surfaces to form nanostructured features. Nanocrystalline metals exhibit improved mechanical properties such as strength, hardness, and wear resistance, compared to their coarser microstructures [1–3]. Among the most common approaches for surface nanostructuring of materials, there are layer deposition techniques such as physical or chemical vapor deposition [4]. In spite of high flexibility in production, these methods may face adhesive bonding issues and a difference in the chemical composition of the deposited layer compared to the underlying substrate. Another interesting approach is the use of severe plastic deformation (SPD) methods, directly applied to the surface, covering the stated issues encountered in the deposition methods.

AISI 316L austenitic stainless steel is widely used in various sectors such as chemical, petrochemical, and food industries, as well as in pharmaceutical and biomedical engineering [5, 6], thanks to its excellent corrosion resistance, work-hardening, and formability. However, compared to some advanced materials, a wider application is constrained by its relatively low mechanical and fatigue strength and poor wear resistance.

In order to achieve desired nanostructured surfaces, SPD has been applied using various techniques such as shot peening [7, 8], laser shock peening [9, 10], surface mechanical attrition treatment (SMAT) [11–13], surface mechanical grinding treatment (SMGT) [14, 15], surface mechanical rolling treatment (SMRT)[16], ultrasonic surface rolling [17], severe impact loading [18], and surface mechanical impact treatment (SMIT)[19]. During the last two decades, these methods were developed and some of them were explored intensively demonstrating the beneficial effects of SPD-based surface nanostructuring on the static strength, wear-resistance, and fatigue durability of metallic materials [20–22].

The improvements in the physical, mechanical, and chemical behavior of metallic materials using surface nanostructuring techniques by relying on the resultant extremely deformed and refined structure have been of broad interest to many researchers. To give examples, Huang et al. [16] used the surface mechanical rolling treatment on AISI 316L austenitic stainless steel to enhance the fatigue properties with the observation that the capability to suppress the initiation of cracks in the deformed surface layer and consequently the fatigue resistance was increased. Another work reported that after laser shock peening of AISI 316L steels, the yield strength was raised significantly due to the blocking of dislocation movement and pining effect [23].

The nanocrystallization mechanism in SPD-based nanostructured metals is through dislocation activities, twinning, and phase transformation [24, 25]. The active mechanism of plastic deformation in metallic materials is strongly determined by the amount of stacking fault energy (SFE) [26]. Formation of dislocation walls and cells due to the dislocation slip is the dominant active deformation mode in materials with high SFE [27]. However, mechanical twinning is the major deformation mechanism in low SFE metals [28]. In other words, in the later materials, the formation of dislocation arrays and twinning is mostly preferred rather than the dislocation cells. For metals with intermediate levels of SFE, a combination of those for low and high SFE materials is usually observed [29]. It was reported that the intersection of twins created the rhombic block from which sub-grains and consequently a nanostructured surface was generated [30]. Jayalakshmi et al. [31] found that twin crossing sub-divided the austenitic grains in AISI 316 steel into finer sub-grains which was also considered as a preferred location for the nucleation of martensite. In AISI 316L austenitic stainless steels with face-centered cubic (FCC) crystal structure and low SFE [32], mechanical twinning accompanied by martensitic transformation play a key role in the deformation and nanocrystallization process [13, 33]. A study carried out by Agrawal et al. [34] demonstrated that the average thickness and distribution of twinning decreased with an increase in the strain rate. However, the number of twins was raised by increasing the strain rate [35].

Also, Bagherifard et al. [7] showed that the work hardening and microhardness of severe shot peened AISI 316L steel were enhanced. In addition to the positive effects of nanocrystallization on mechanical properties, it has been found that the thermal stability of nanotwinned AISI 316L steel could be increased up to 800 °C [36]. After the application of ultrasonic impact treatment (UIT) on different types of carbon steel, the thickness of the plastically deformed layer varies from a few microns to about 100 μm depending on the duration of UIT. Obvious grain refinement was observed and the grain size was about 10 nm in the top surface layer. Accordingly, the microhardness of the surface

layer was enhanced significantly; the hardness increased as a function of UIT duration [37]. It was reported that by the application of shot peening, the surface nanostructured AISI 316L samples exhibited considerable enhancement in mechanical properties and fatigue behavior, as well as an increase in enzymatic activity which promoted the application of surface nanocrystallized samples for biomedical and biochemical applications [38]. Li et al. [14] used the SMGT to prepare a spatial gradient nanograin structured surface layer on a bulk Cu rod and improved the hardness through significant grain refinement.

The aforementioned concise literature review indicates the significance and the high effectiveness of SPD-based surface nanostructuring in the enhancement of the structural integrity of materials and related components. Accordingly, the development of novel techniques capable of generating such nanostructured surfaces remains a challenging and essential demand. In a previous study, Dehghan et al. [19] developed a novel surface nanostructuring technique called SMIT. It was demonstrated to be very efficient for the microstructure refinement and enhancing the mechanical performance of the treated samples. Herein, the surface nanostructuring and resultant microstructural modifications and mechanical performance of AISI 316L austenitic stainless steel were investigated using this novel technique. To this aim, a sheet of material with 1 mm thickness was treated with various processing parameter combinations. The effectiveness of the treatment was evaluated by characterizing the microstructure using X-ray diffraction, transmission electron microscopy, optical microscopy, and field emission scanning electron microscopy, as well as the structural integrity using micro-indentation and tensile testing. A detailed examination of the microstructural features along the depth of the material is given. A comprehensive discussion is provided to establish a proper connection between experimental data and the available data in the literature.

2 Material and Experimental Procedures

2.1 Process Principles and Sample Preparation

The process and the relevant setup to synthesize a nanostructured surface layer are explained in this section. Owing to the implemented principles which are based on the successive impacts of hard balls, this process is named "surface mechanical impact treatment" or briefly, SMIT. The principles of the SMIT along with the custom-built setup are illustrated in Fig. 1. This device consists of two strong electromagnetic coils at the top and bottom of an oscillator that provides the driving force for the impact. Electric current is applied in a pulse form to the coils which in turn, causes the oscillator to move up and down. The oscillator is connected

to a piston in which the balls are placed and are in contact with the sample surface during the treatment. The intensity of SMIT can be adjusted with the applied voltage to the electromagnetic coils. As the voltage increases, the amount of applied current through the coils increases, which increases the electromagnetic force, resulting in a higher speed of the oscillator and thus higher intensity of the process. While more similarities may be found between SMIT and SMAT processes, the most important difference is in the impact mechanism. In SMAT, balls are flying in the chamber and impact with high speeds while in SMIT, they are vibrating in their position with high frequency.

A commercial AISI 316L austenitic stainless steel sheet with an average thickness of 1 mm was investigated in the present study. The initial material was cut into samples with a dimension of $30 \times 80 \text{mm}^2$ and was annealed at 1050 °C for 3 h under the protected argon atmosphere.

The samples were treated at room temperature using a voltage of 90 V and for various durations of 0.5 h, 1.0 h, and 2.0 h. Stainless steel balls with a hardness of 800 HV and a diameter of 3.5 mm and 5.0 mm were utilized as the treating media. About 90% of the chamber area was filled with balls in order to provide a uniform deformation as well as free movement of the balls. The use of larger or smaller balls was not possible with this version of the SMIT machine due to technical limitations in the setup design. The processing parameters for the treated samples are summarized in Table 1. The treated samples were named according to the ball size and treatment duration. Thus, the sample 5.0–0.5 indicates the treated sample with a 5.0 mm ball for 0.5 h, etc. Both sides of the samples were treated successively.

2.2 Microstructural Characterization

After SMIT, smaller specimens were cut and englobed in resin. The specimens were mechanically ground and polished using 0.3-micron diamond paste, and then etched with a solution of 50% HCl, 15% HNO_3, and 35% H_2O. The cross-sectional microstructure of the samples was characterized using OLYMPUS BX51M optical microscope and FEI Nova NanoSEM 450 field emission scanning electron microscope (FESEM) operated at a voltage of 15 kV.

Transmission electron microscopy (TEM) observations and selected area electron diffraction (SAED) studies were carried out using an FEI Tecnai G2 F20 SuperTwin system with an accelerating voltage of 200 kV. The plane-view TEM samples were prepared from the top surface layer (depth of ∼ 10 μm) of the treated samples by mechanically grinding them into a foil of ∼ 50 μm in thickness and finally dimpling and ion-milling for perforation purposes.

A Philips X'Pert MPD X-ray diffraction (XRD) measurement system (40 kW) with Co Kα radiation was used to determine phase constitutions and SFE in the treated surface

Fig. 1 **a** Schematic illustration of the SMIT setup, (1) electromagnetic coils, (2) oscillator, (3) piston, (4) balls, (5) sample, (6) liquid nitrogen chamber **b** piston positioning before and during impact **c** custom–built setup
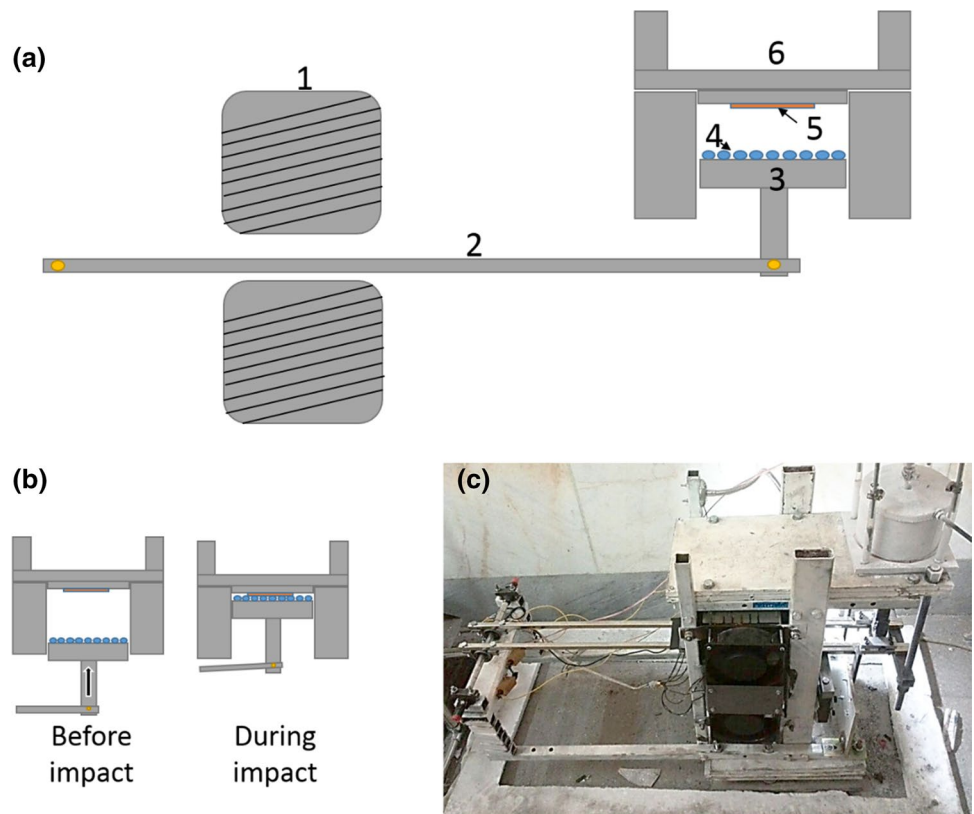

Table 1 SMIT processing parameters

Sample	Time (h)	Ball diameter (mm)	Voltage (V)	Frequency (Hz)
Not SMITed	0	–	–	–
5.0–0.5	0.5	5	90	5
5.0–1	1	5	90	5
5.0–2	2	5	90	5
3.5–0.5	0.5	3.5	90	5
3.5–1	1	3.5	90	5
3.5–2	2	3.5	90	5

layer. Also, the grain size was determined by Williamson-Hall analysis [39]. Small angular steps of $2\theta = 0.02°$ and diffraction angles between $40° \leq 2\theta \leq 130°$ were used to capture the intensities of diffraction peaks in the step-scanning mode.

The SFE of the treated samples was measured using recorded XRD spectra. This method has been implemented by Reed and Schramm [40] to determine the SFE of several austenitic stainless steel alloys. The SFE calculation is based on the measurement of the stacking fault probability (SFP) from the shift in the XRD peaks while the mean-square microstrain is assessed through the XRD line broadening.

Using the microstrain and SFP, it is possible to determine the SFE (γ):

$$\Upsilon = \frac{k_{111}\omega_0 G_{(111)}\alpha_0 A^{-0.37}}{\pi\sqrt{3}} \frac{\langle\varepsilon_{50}^2\rangle_{111}}{\alpha} \tag{1}$$

where $K_{111}\omega_0 = 6.6$ is the proportionality constant, $G_{(111)} = \frac{1}{3}(C_{44} + C_{11} - C_{12})$ is the shear modulus in the (111) fault plane, α_0 is the unit cell edge dimension, A is the Zener anisotropy equal to $2C_{44}/(C_{11}-C_{12})$, and C_{ij} is elastic stiffness coefficients [40], α is the SFP, and $\langle\varepsilon_{50}^2\rangle_{111}$ is the mean-square microstrain. To calculate SFE using Eq. (1), it is necessary to know the parameters. Based on the literature [40], the average values of the parameters for all steel types are as the following: $G_{(111)} = 0.65 \times 10^{11}$ N/m^2 and A = 3.43. The lattice parameter of AISI 316L steel is 3.589 Å and was obtained from XRD analysis. Equation (1) then reduces to:

$$\gamma = 17979 \frac{\varepsilon_{50111}^2}{\alpha} (\text{mJ/m}^2) \tag{2}$$

In this equation, α is calculated based on the peak shift and $\langle\varepsilon_{50}^2\rangle_{111}$ is averaged over the distance of 50 Å; this can be considered equal to the general microstrain obtained from the Williamson-Hall analysis [41]. To calculate the microstrain for each sample, the peak shift was compared with the untreated sample in the as-annealed condition.

Stacking faults in an FCC crystal occur on (111) closed-pack planes. To avoid diffractometer zero errors and to increase sensitivity, the profile angular separation of (111) and (200) reflections rather than the absolute 2θ positions was used. Thus, SFP (α) was calculated through Eq. (3) [42]:

$$\alpha = \frac{\Delta(2\theta_{200} - 2\theta_{111})}{-45\sqrt{3}\left(\tan\theta_{200} + \frac{\tan\theta_{111}}{2}\right)}\pi^2 \tag{3}$$

where $\Delta(2\theta_{200} - 2\theta_{111})$ can be measured using Eq. (4):

$$\Delta(2\theta_{200} - 2\theta_{111}) = \Delta(2\theta_{200} - 2\theta_{111})_{deformed} - \Delta(2\theta_{200} - 2\theta_{111})_{annealed} \tag{4}$$

2.3 Mechanical Tests

Uniaxial tensile tests were performed on an Instron 5600 testing machine with a strain rate of 6×10^{-4} s^{-1} at room temperature. The geometry of the miniature tensile test specimen is given in Fig. 2. [43]. The specimens had the same thickness as the initial sheet with both faces treated with SMIT.

Vickers microhardness test was performed on the cross-section of the samples using a Buehler Micromet hardness tester equipped with a Vickers indenter using a load of 50 g and a dwell time of 20 s. Hardness measurements were repeated three times. The distance between any two neighboring indentations was kept at around 50 μm to ensure the validity of the measurements.

3 Results

3.1 Microstructure of the SMIT Surface Layer

Figure 3 shows the microstructures of the untreated AISI 316L stainless steel sample in the core as well as the surface region which consists of primarily equiaxed grains (~50 μm in size) with few annealing twins. The flow lines near the surface are left from the manufacturing process of the sheet. However, they do not contribute to the deformations as the sheet was annealed before SMIT. Figure 4a–f show the optical microscopic (OM) images of the SMIT samples treated on both sides. Clear evidence of the plastic deformation and microstructure refinement is observed in the total thickness of the SMITed samples with 1 h and 2 h treatments. The grains in the core (away from the surface) have remained equiaxed in shape and a large number of deformation twins and multiple slip bands are visible. The twining density increases with a decreasing depth from the surface. Near the surface, the microstructure is severely deformed and is hardly identified using OM (Fig. 4c, f).
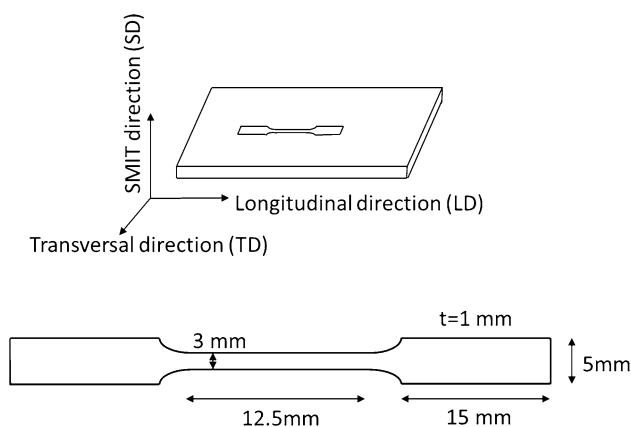

Fig. 2 Geometry of miniature tensile test specimen (t = thickness)

Figure 4a depicts the microstructure of the specimen treated with a ball size of 3.5 mm and a duration of 30 min. As can be seen, a high density of deformation twins is observed within the austenitic grains and the deformation twin density is higher at the treated surface. Within some grains, the presence of multiple twin systems constructed a network pattern indicating dislocation accumulation. Figure 4b, c show the microstructure of the sample treated with the same ball size for 1 h and 2 h, respectively. It can be seen that after 2 h of treatment, the deformation twins are formed in a greater depth (about 400 μm in Fig. 4c, f). By increasing the size of the ball, the density of the grains with irregular multiple-twins was gradually increased (see Fig. 4d). As shown in Fig. 4e, f, by increasing the treatment time, the depth of the deformed layer and the density of the twins have increased.

The microstructure of SMIT samples taken by FESEM is shown in Fig. 5a–f. Rectangular blocks or rhombic blocks are observed in all the samples near the treated surface. These blocks are formed by the intersection of two systems of parallel twin lamellae. With a ball size of 3.5 mm, the number of rhombic blocks increases with increasing treatment time, and their sizes become smaller, as shown in Fig. 5b, c. Several twinning systems could be observed in specific grains. However, deformation twins are not present within all the grains at the core of the samples, which shows that the formation of deformation twins is closely related to the orientation of grains or the amount of applied strain. Figure 5a–f demonstrates that regardless of the SMIT time, the closer the twins are to the treated surface, the denser they become. Also, the grains are refined by rhombic blocks. The same features of deformation are observed in the samples treated with a ball size of 5.0 mm, as depicted in Fig. 5d–f.

FESEM images of SMIT samples at larger magnifications with a treated condition of 3.5–2, 5.0–1, and 5.0–0.5 are shown in Fig. 6a–d, depicting the formation of stacking fault tetrahedra (SFT) in the treated samples. Figure 6a shows the

Fig. 3 Microstructure of AISI 316L stainless steel before SMI treatment **a** in the sample core **b** near the surface
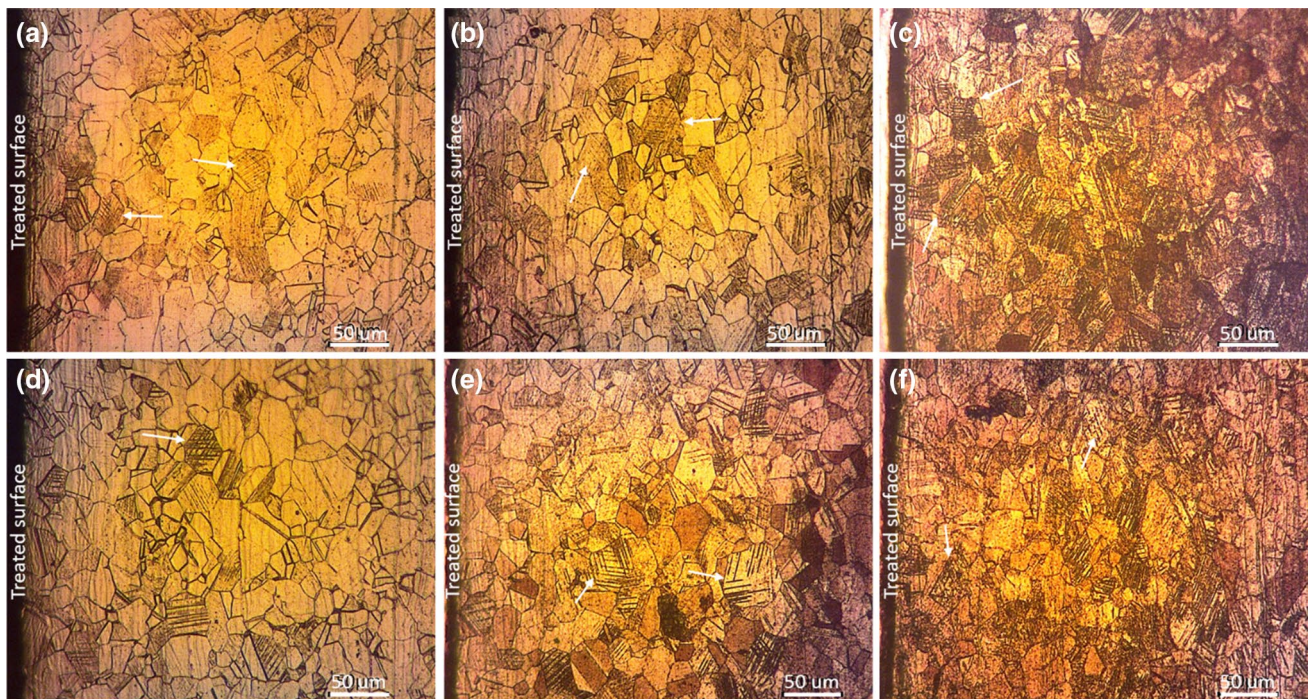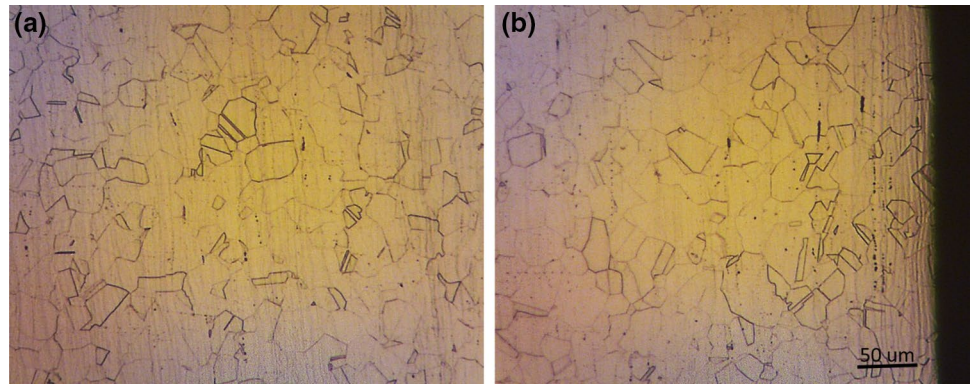

Fig. 4 Cross-sectional OM images of the SMIT samples and deformation layer depth in **a** 3.5–0.5, **b** 3.5–1, **c** 3.5–2, **d** 5.0–0.5, **e** 5.0–1 and **f** 5.0–2. White arrows show the multiple twin systems in a single grain

SFT formed on the deformation twins. In Fig. 6b, SFTs are formed on the deformation twins with a high density. Figure 6c, d show the high density of the SFTs formed inside the grains or at the grain boundaries. Due to the fact that grain boundaries, slip bands, and twins are the preferred sites of dislocation absorption, the formation of SFTs on these sites is expected [44]. The SFTs formed by SMIT appear to have dimensions even larger than 1 μm that are easily detectable using FESEM. To the best of the authors' knowledge, SFTs with such large dimensions were not reported previously and were observed to be in the submicron range [44, 45].

TEM micrographs in Fig. 7 characterize the microstructure evolution in the subsurface layers which is 20–30 μm deep from the treated surface. Compared to the original

microstructure that mainly consisted of austenite grains, the SMIT processed samples are characterized by multi-feature microstructures. In the 5.0–0.5 specimen (Fig. 7a–d), typical microstructures contain slip bands (Fig. 7a, b) and twins with a nanosized thickness (Fig. 7c, d). In Fig. 7a a high density of dislocations and dislocation tangles and slip bands of several systems can also be observed. Their intersections formed blocks with a size equal to the slip band/matrix lamellar thickness (~70 nm) and have caused the fragmentation of grains into refined blocks (Fig. 7b). The intersections of these slip bands usually serve as nuclei of α' martensite. An appropriate SAED pattern shows the existence of α' martensite at the intersection of two slip bands (inset in Fig. 7b). In Fig. 7c–d, nano-scaled twins are formed in their parent
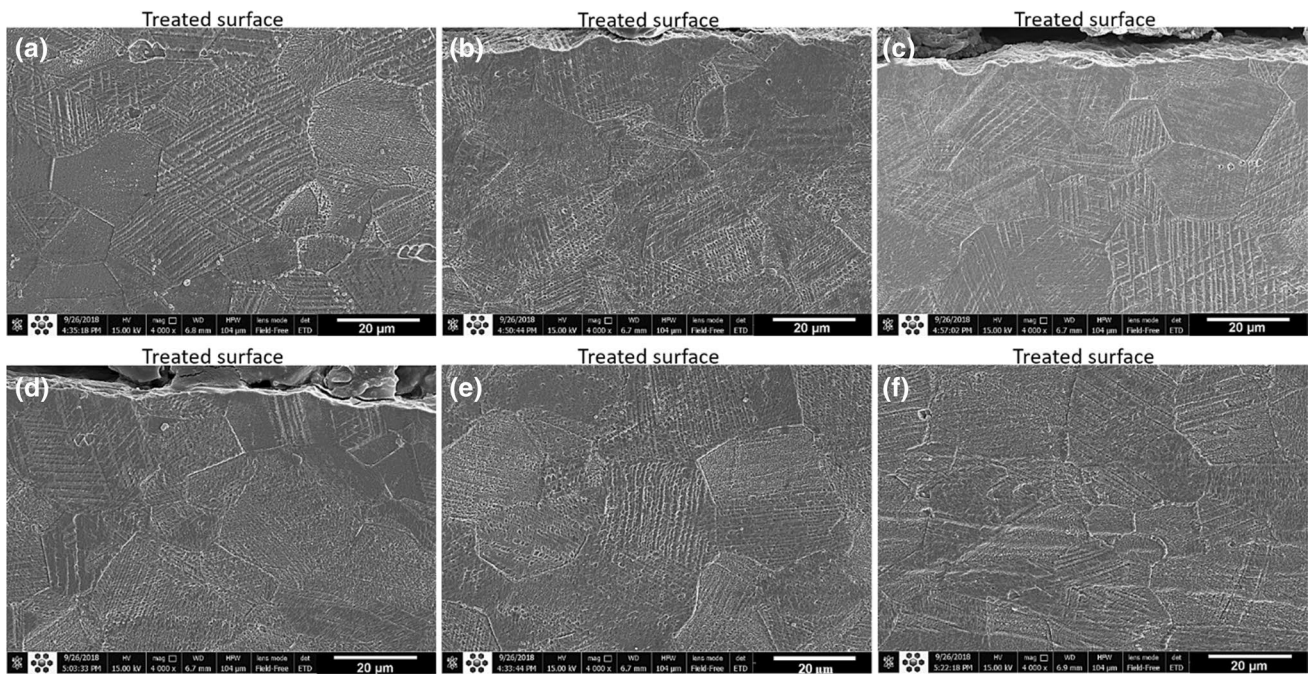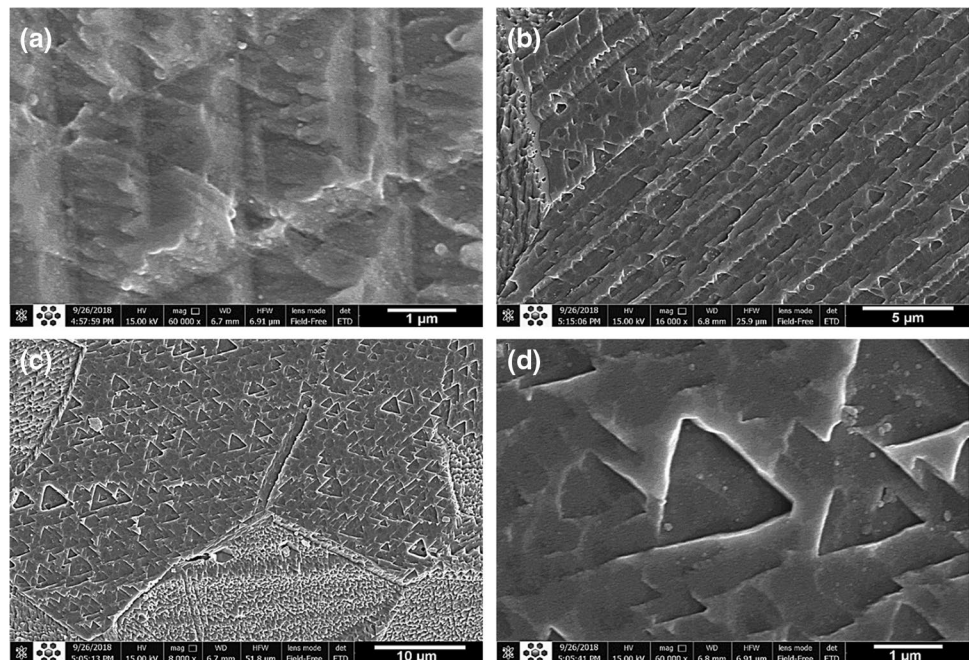
Fig. 5 FESEM images of SMIT samples showing the interception of twinning in the near the treated surface of samples: **a** 3.5–0.5, **b** 3.5–1, **c** 3.5–2, **d** 5.0–0.5, **e** 5.0–1 and **f** 5.0–2

Fig. 6 FESEM image of SFT formation in SMIT samples on the deformation twins in 3.5–2 **a** and 5–1 **b** and in grain and grain boundaries of 5.0–0.5 h **c, d**

grains as indicated in the SAED pattern (inset in Fig. 7c) with a large number of dislocations. A high density of dislocations can also be seen inside the twins and near their boundaries. An arrangement of these dislocations results in the formation of walls within the microtwins while others are arranged into planar arrays which are mainly typical of

materials with low SFE during plastic deformation. As an additional deformation process, twinning competes with dislocation activities as the strain increases. Besides the presence of deformation twins, the SMITed samples contain many stacking faults (SF) as shown in Fig. 8a, consistent with the calculated value of the SFE (Sect. 3.2). In Fig. 8b, a

Fig. 7 Bright-field TEM images of the SMIT 5.0–0.5 specimens (processed for 30 min with the 5 mm balls) depicting: **a** slip bands formation inside the grain, **b** higher magnification of the indicated area in **a** with the relevant SAED pattern (inset in **b**), **c** and **d** deformation twins with SAED pattern (inset in **c**)
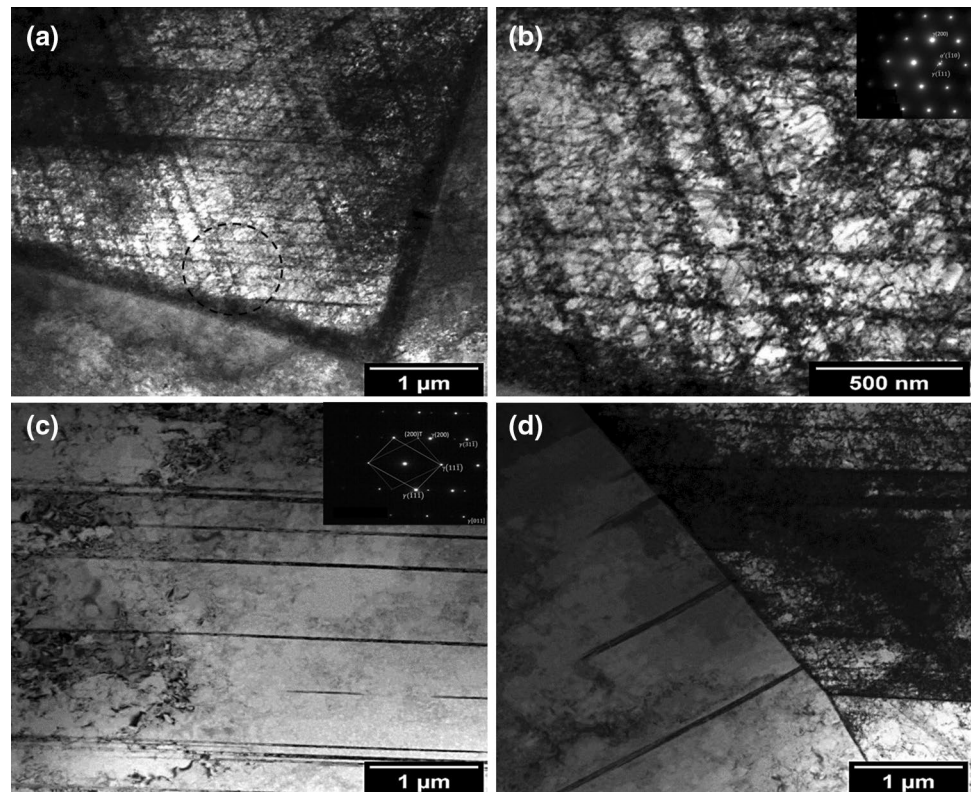
high density of dislocations, dislocation tangles, and SFs can be observed and the corresponding SAED pattern (Fig. 8d) shows that the selected area in Fig. 8c consists mainly of FCC γ-austenite phase.

Areas with well-formed dislocation cell structures can be seen in the SMIT processed specimen (5.0–0.5) (Fig. 9a). The average cell size ranges from 50–200 nm (Fig. 9a–c). When the SMIT process proceeds, the extremely twinned/slip banded areas coexist with the areas of the well-formed dislocation tangle and walls (Fig. 9b) and nanosized sub-grains/grains (Fig. 9c).

In FCC metals, SFTs are common defects generated by processes such as irradiation [46, 47], aging after quenching from temperatures close to the melting temperature [48, 49], and SPD [50, 51]. Figure 10 shows SFT formed during the SMIT process. SFTs with a size of 30–50 nm are formed on {111} planes and edges are parallel to ⟨110⟩ directions within regions where there is a high dislocation density. These observations strongly suggest that the SFTs could not be formed by clustering of vacancies and thus, a dislocation mechanism must be responsible. Figure 10a depicts the SFT of the specimen treated with a ball size of 3.5 mm and a duration of 30 min. Figure 10b, c shows the SFT of the sample treated with the same ball size for 1 h and 2 h, respectively. It can be seen that the number of formed SFTs has increased with an increase in the treatment time. The images presented in Fig. 10d, e show the SFT and their

interaction with a dislocation line in SMIT samples with 5.0–0.5 and 5.0–1, respectively. This suggests that the dislocation bypasses the tetrahedra by cross-slip. Figure 10f shows dark-field TEM observations of SFT formation in the 5.0–2 sample.

3.2 SFE and Microstructure Evaluation by XRD Analysis

Martensite induced by deformation in the SMIT surface layer was identified using XRD analysis. The annealed sample is solely composed of the austenite phase and no peaks regarding the martensite phase can be seen in the XRD pattern (see Fig. 11a). Three phases were reflected in the diffraction pattern of the SMIT processed specimens. This implies that the microstructure of the surface layer of the specimen contains the austenite and two strain-induced martensitic (ε and α′) phases. It should be noted that due to an increase in the volume fraction of induced martensite as a function of SMIT time, diffraction peaks such as 211 are not easily detectable at a treatment time of 0.5 h but are intensified at larger SMIT times.

The formation of ε and α′ martensite strongly depends on the steel composition and related SFE. With decreasing SFE, the austenitic lattice becomes more sensitive to the formation of ε [23]. The calculated SFE value from XRD measurements for SMIT samples is presented in Table 2. Low
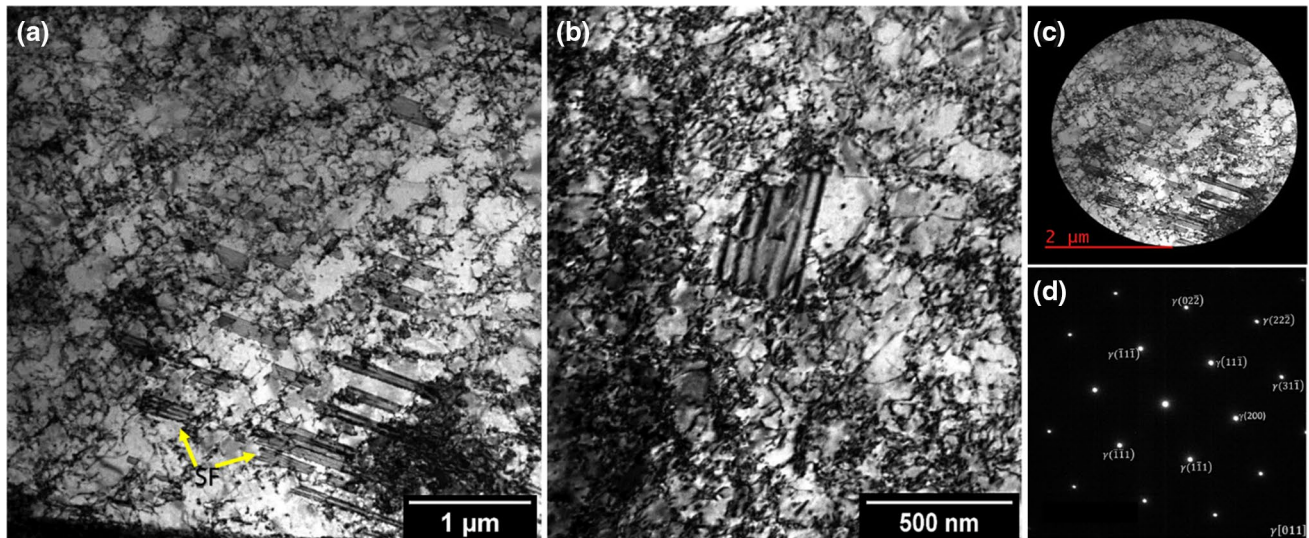
Fig. 8 **a** Bright-field TEM image of the SMIT 5.0–0.5 sample (processed for 30 min with 5 mm balls). Yellow arrows indicate SFs. **b** same as **a** with a high density of dislocations and dislocation tangles showing SF formation. **c** an area selected from **a**. **d** SAED pattern of the area indicated in **c**
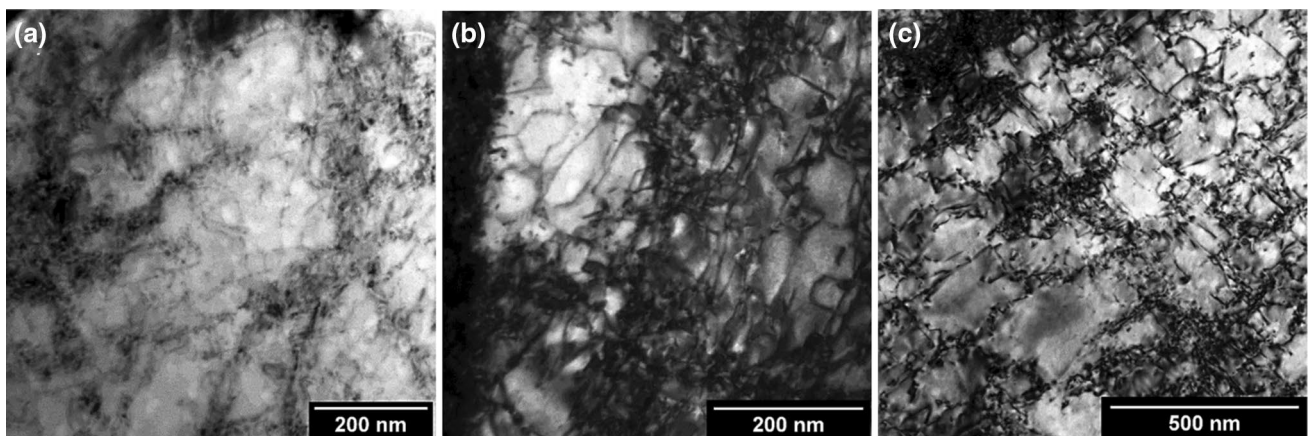

Fig. 9 Bright-field TEM images of the specimens processed for 30 min using 5 mm balls (5.0–0.5) showing: **a** Dislocation cells, **b** Dislocation tangle/dense dislocation walls, **c** Nanosized subgrains/grains

SFE is known to promote deformation-induced martensite (DIM) during straining. The formation of martensite (e.g. Transformation-Induced Plasticity effect) is predominant when the SFE of austenite is less than ~20 mJ/m^2 [52]. The alloys with low SFE tend to form planar structures through dislocation slipping because of more difficult cross slip [53]. The deformation twins begin to form to accommodate further deformation. Here, twinning is one of the deformation mechanisms. The grains are refined and further subdivided by twins. It is noted that the calculated SFE values by the XRD method, which are one to two orders of magnitude lower than expected [54], are prone to errors and are normally suggested to be multiplied by modification factors in the range of 10–100 [55]. Thus, the calculated SFE values should be considered with a modification factor of 10 to 100.

3.2.1 Evaluation of Grain Size, Lattice Microstrain and Dislocation Density by XRD

The grain size was calculated on the surface layer of each sample using XRD. In XRD analysis, the grain size (D) and microstrain (ε) were related to peak broadening of XRD peaks using different fitting functions like Gaussian, Cauchy, and Pseudo-Voigt (incorporating both the Gaussian and Lorentz functions) based on the Williamson-hall equation and the Voigt method with most high reliability factor (R^2)
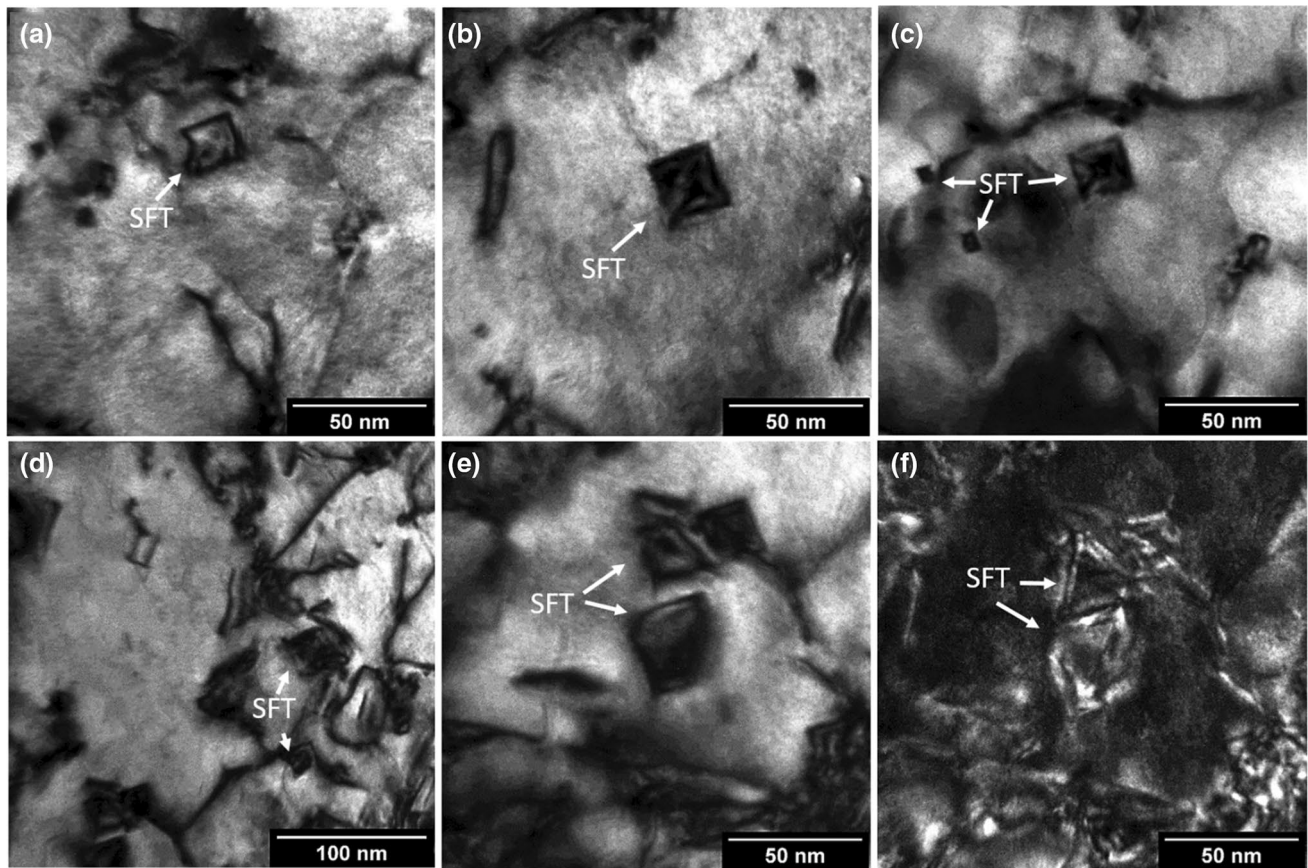
Fig. 10 Bright-field TEM of SFT in SMIT samples with **a** 3.5–0.5, **b** 3.5–1, **c** 3.5–2, **d** 5.0–0.5, **e** 50.-1 and **f** dark-field TEM observations of SFTs (arrowed) in the SMIT processed specimens for 120 min with the 5 mm balls (5.0–2). Images are taken near the zone axis $B = \langle 100 \rangle$ using the reflecting plane vector g = 020

was reported. Estimations of dislocation densities (ρ) in the original and deformed samples were performed using the values of D, ε, and Burgers vector b based on Eq. (5) [56]:

$$\rho = 2\sqrt{3}\varepsilon/Db \tag{5}$$

A Burgers vector of 0.25 nm was chosen according to the literature [56]. Table 3 shows the calculated grain size, lattice microstrains, and dislocation density of the SMITed specimens. The estimated mean grain size is around 20 nm.

The provided data in Table 3 are depicted in Fig. 12 for a better presentation of variable changes with the treatment time. Refinement of the grain size down to 20–30 nm has already occurred upon the application of SMIT for 30 min and continuation of the process hardly decreases the grain size (Fig. 12a). Lattice microstrains significantly affect the broadening of the diffraction profiles. The most noticeable lattice microstrains are observed for 0.5 h SMIT processed specimens (Fig. 12b). Taking into account the approximated values of the grain size D, lattice micro-strains ε, and the dislocation

densities ρ were also computed with ongoing deformation at the SMIT process (Fig. 12c). It is seen that higher ρ occurs after 2 h using SMIT process.

3.3 Mechanical Properties of the SMIT Samples

Microhardness measurements on the cross-section of the SMIT surface were determined as shown in Fig. 13. The microhardness reaches a maximum value of ~650 HV at both the topmost treated surfaces and decreases gradually toward the core value (~220 HV) in the middle of sample thickness (at a depth of ~500 μm). An increase of 200% in microhardness in the surface of SMIT samples is notable in comparison with those achieved by other surface treatment methods, such as SMAT [20], shot peening [57], and laser peening [58]. Moreover, microhardness variations along the cross-section are of the gradient type and gradually increase from 220 to 650 HV, and further verify that a gradient microstructure of grain or cell size, martensite fraction, and dislocation density was formed on the SMIT surface layer. In addition to the grain refinement effects, a
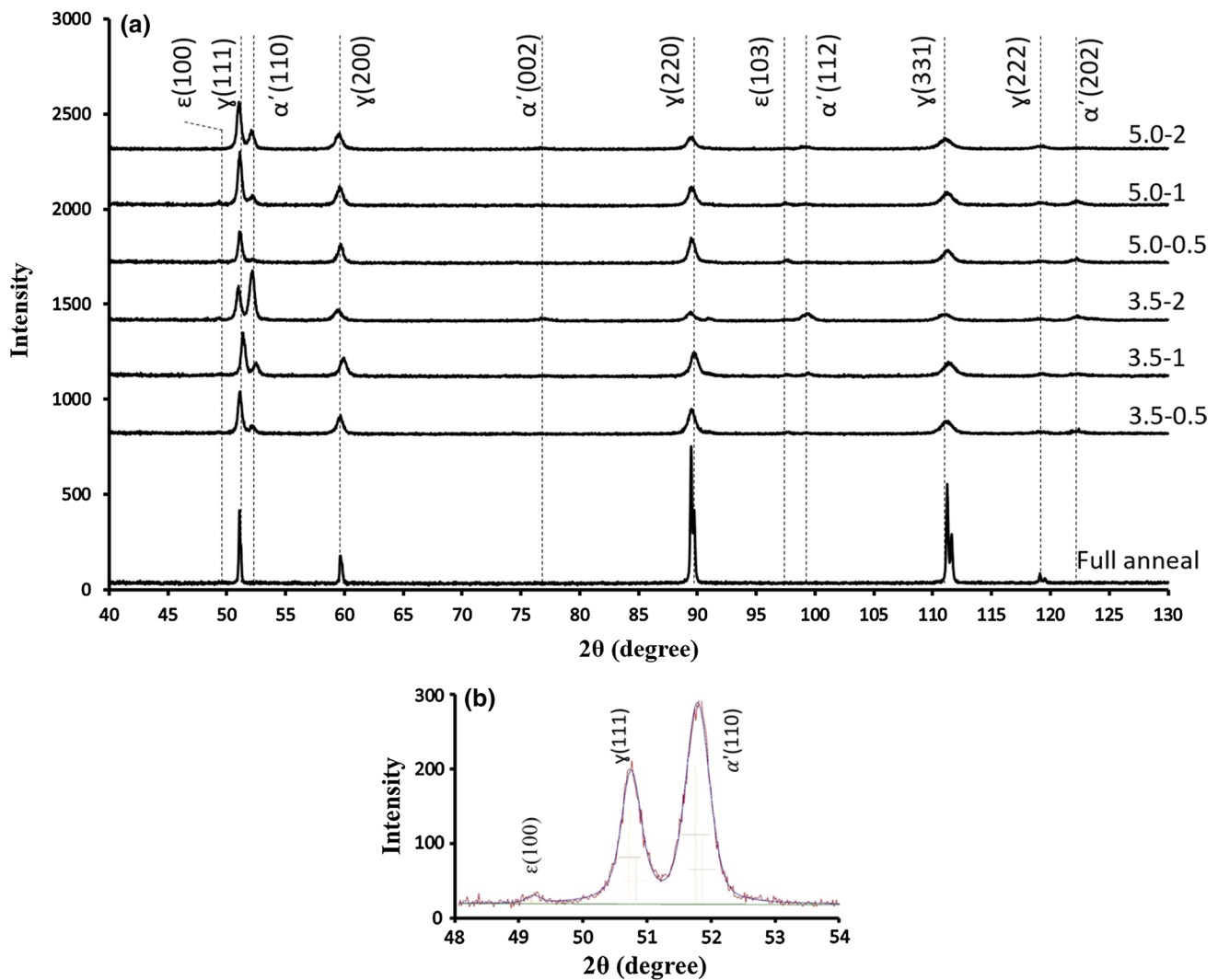
Fig. 11 a Recorded XRD profiles **b** magnified XRD pattern of sample 3.5–2 highlighting the peaks for the existence of ε and α′ martensite in SMIT samples

Table 2 Mean square microstrain, stacking fault probability, and stacking fault energy of SMITed samples obtained by XRD

sample	Stacking fault probability $10^3\,\alpha$	Microstrain $10^6\langle\varepsilon_{50}^2\rangle_{111}$	Stacking fault energy (γ) (mJ/m^2)
5.0–0.5	9.3	0.77	1.49
5.0–1	16.8	0.7	0.75
5.0–2	10.3	0.64	1.11
3.5–0.5	16.7	0.72	0.77
3.5–1	14.8	0.18	0.22
3.5–2	24.4	3.34	2.47

Table 3 calculated grain size, lattice microstrains, and dislocation density of the SMITed samples based on XRD analysis

ρ (m^{-2}) (10^{14})	R^2	Microstrain %	grain size (nm)	sample
0.0000194	0.95	0.007	50,000	Not treated
5.81	0.75	0.088	21	5.0–0.5
6.03	0.83	0.084	19.3	5.0–1
6.56	0.72	0.018	18.6	5.0–2
6.81	0.81	0.085	17.3	3.5–0.5
3.19	0.87	0.043	18.7	3.5–1
18	0.91	0.046	17.9	3.5–2

higher concentration of martensite phase (see discussion) resulted in a much higher hardness at the top surface. Figure 13a shows the microhardness of 3.5–0.5, 3.5–1, and 3.5–2 samples. As it can be seen, with increasing SMIT

time, the hardness increased. Moreover, hardness increased due to the increasing size of the balls (Fig. 13a, b). It is noted that as a result of severe deformation, the thickness of the sample decreases with increasing time. Also, the successive
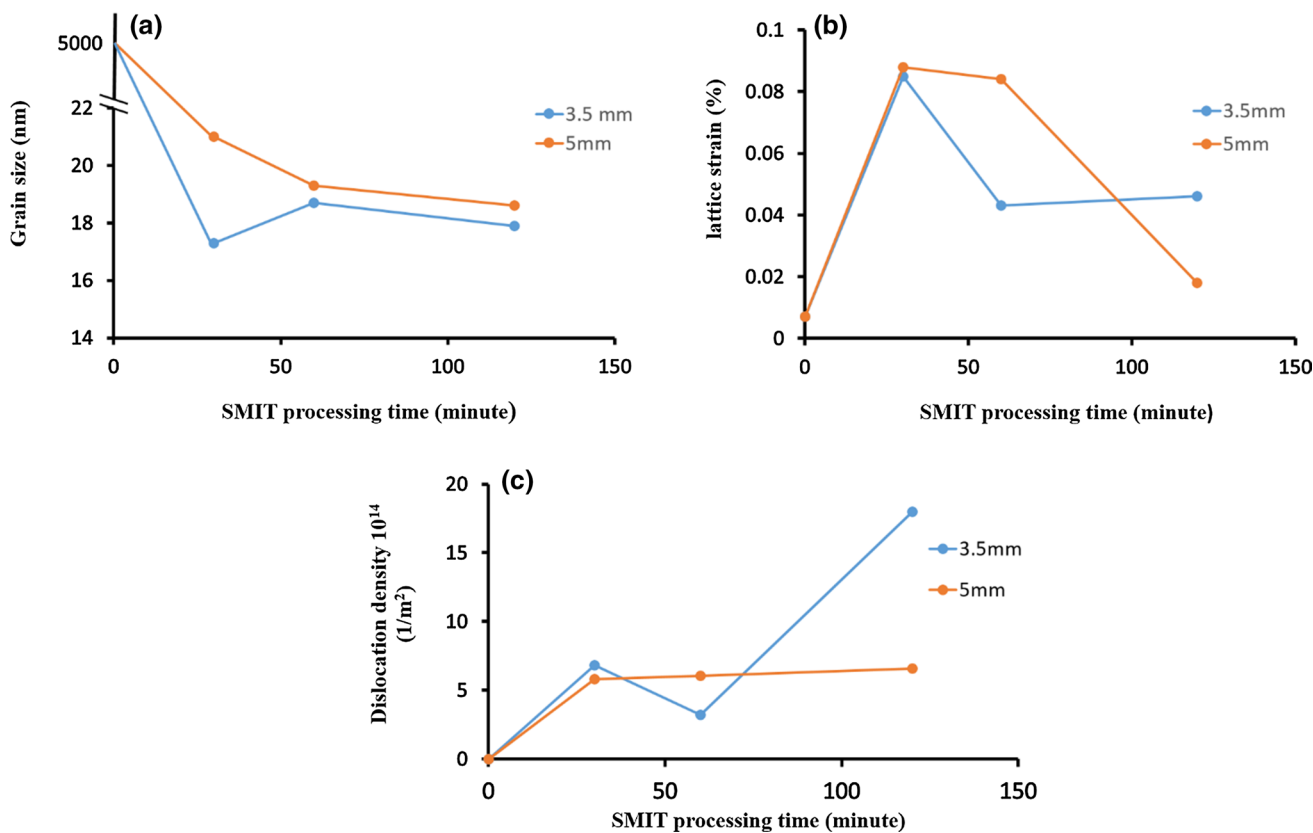
Fig. 12 Dependencies of the grain size **a**, lattice micro-strain **b**, and dislocation densities **c** of SMIT processed specimens on the processing time using XRD analysis

treatment on both sides of the sample produced an asymmetry in the hardness profile with respect to the sample center, especially in the case of 5 mm ball.

Uniaxial tensile engineering stress–strain curves of the SMIT samples with a gauge length of 12.5 mm, 3 mm width, and 1 mm in thickness are shown in Fig. 14. It is noted that the stress distribution from the surface to the core of the

sample is gradient, thus the amount of stress in the SMIT samples indicates the average values obtained from the analogous uniaxial tensile force and initial cross-sectional area of the tested sample in the current study. In comparison with the coarse-grained sample in the sample with the most severe SMIT conditions (3.5–2), the amount of yield stress and ultimate strength increased from 250 and 550 MPa
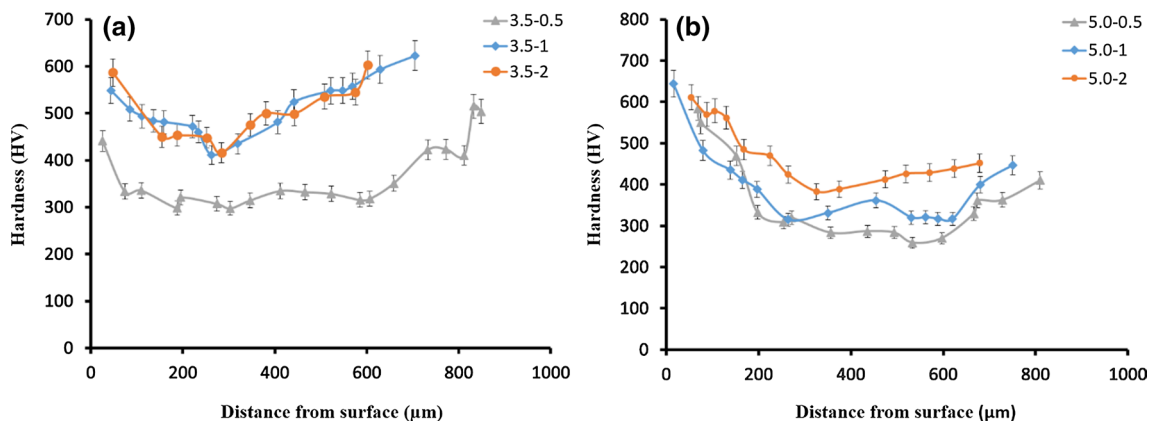

Fig. 13 Variations of microhardness with distance from treated surfaces of the SMITed samples with **a** 3.5 mm balls at 0.5 h, 1 h and 2 h and **b** 5 mm at 0.5 h, 1 h and 2 h

to about 720 and 730 MPa, respectively. Meanwhile, the homogenous elongation decreased from ~120% to ~20%. The strength increase in SMIT samples is related to the severely grain nanostructured surface layer and deformed sub-surface layer as a result of grain refinement and martensite formation. A yield strength as high as 1450 MPa has been observed in the nanostructured AISI 316L steel (with an average grain size of 40 nm) treated by SMAT [59]. Figure 14a shows the stress–strain curves of SMIT specimens with 3.5 mm balls. It is observed that with increasing process time, yield stress and ultimate strength increase, and the uniform elongation decreases. There was some strain hardening during the plastic deformation prior to fracture. However, after the yield point, the slope of the rate of work hardening decreases due to a very low storage efficiency of dislocation within fine grains. Meanwhile, this weak strain hardening is also representative of some lattice dislocation accumulation that occurred during plastic straining before failure. Figure 14b shows the stress–strain curves for SMIT specimens with 5 mm ball size. The measured values of yield stress and ultimate strength and elongation for the SMIT samples with different conditions are given in Table 4.

3.4 Fractography of SMIT samples

Figure 15 a–i and 16 a–i show the fracture surface morphologies of the SMIT samples with 3.5 mm and 5 mm balls, respectively, after the tensile testing. Two kinds of fracture patterns were observed in the SMIT samples, marked as 1 and 2, because of the change of microstructure along the depth from the treated surface. Two apparent failure structures are clearly distinguished on the two outer sides of SMIT samples. One pattern associated with the treated surface containing the refined area shows very few dimples in the flat fracture surface region (Figs. 15 b, e, and h and 16 b, e, and h). In Figs. 15 and 16, a magnified view of the two areas is presented, depicting obvious transition morphology in regions 1 and 2 in which region 1 is characterized by a brittle failure mode. While the pattern in region 2 which is related to the sample core with a larger grain size, presents a heavy cup and cone morphology (Figs. 15 and 16c, f, and i), suggesting that the SMIT samples have been torn apart via a

ductile mode that leads to the observed plasticity indicated earlier in Fig. 14a–b. Combined with tensile testing results, the brittle failure of both surface layers is suppressed by the ductile middle portion of the samples. Therefore, the fracture mechanism observed on both sides can be related to the gradient structure of the SMIT samples.

4 Discussion

In a recent study [19], a new process named as surface mechanical impact treatment (SMIT) was introduced for the surface nanocrystallization of metallic materials. SMIT is originally intended to improve the strength of metals by generating nanocrystallites at the surface layer of the treated material. In the current study, it was applied to AISI 316L stainless steel incorporating various processing parameters such as ball size and treatment time to investigate the capability of the process in surface nanostructuring of AISI 316L stainless steel. The SMIT induced the formation of a severely deformed surface layer with an average grain size of 17–21 nm on AISI 316L stainless steel. Compared with the previous surface mechanical treatment methods such as SMAT [60], shot peening [61, 62], and surface mechanical rolling treatment (SMRT) [16], SMIT generated a comparable deformation layer. Typically, the microstructure-refined layers produced by SMIT are sufficiently thick due to high accumulated strains. Due to a different energy transfer mechanism

Table 4 Mechanical properties of SMITed samples with different processing parameters

Elongation (%)	UTS (MPa)	Yield strength (MPa)	sample
120	630	280	Not treated
15.17	670	510	3.5–0.5
16.1	745	590	3.5–1
5.7	730	700	3.5–2
20.6	670	440	5.0–0.5
15.38	680	470	5.0–1
13.28	740	650	5.0–2

Fig. 14 Tensile engineering stress–strain curves of the coarse grain sample and the SMIT samples treated with **a** 3.5 mm ball **b** 5 mm ball
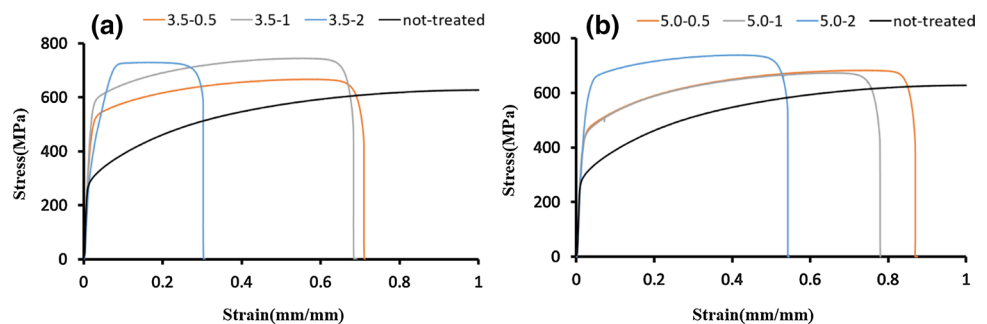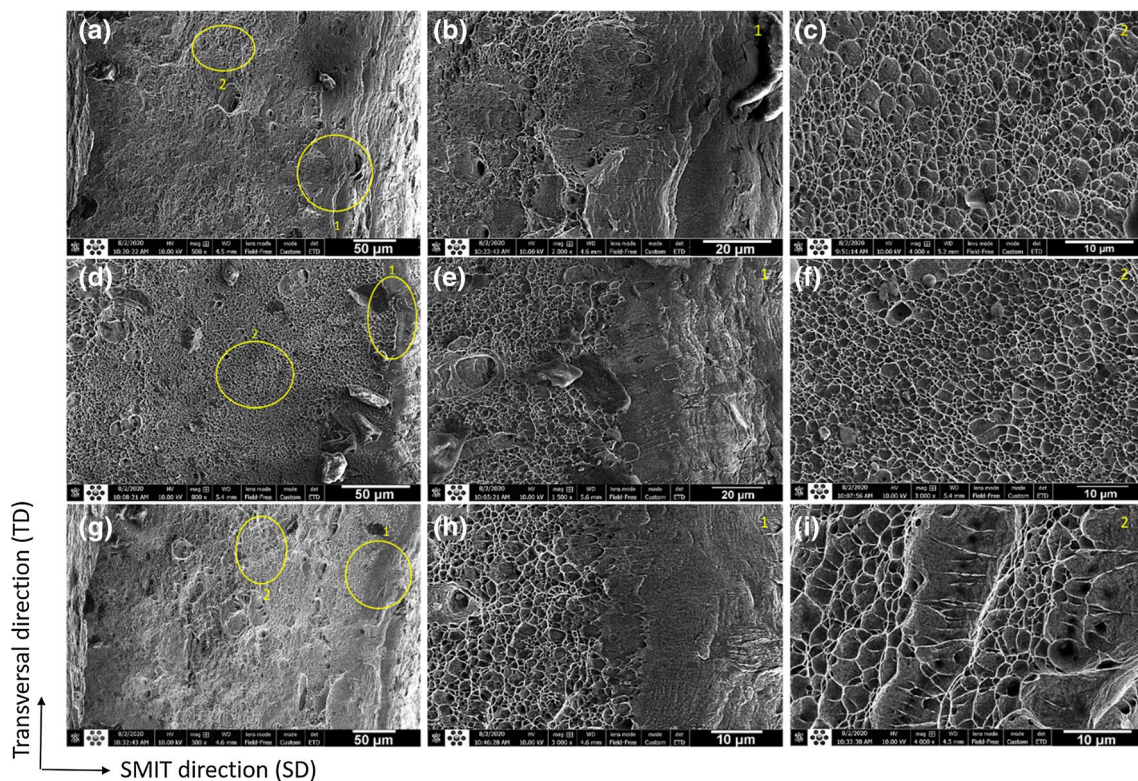
Fig. 15 **a** Fracture surface morphology of 3.5–0.5 sample, **b** higher magnification of region 1 in **a**, **c** higher magnification of region 2 in **a**, **d** fracture morphology of 3.5–1 sample, **e** higher magnification of region 1 in **d**, **f** higher magnification of region 2 in **d**, **g** fracture morphology of 3.5–2 sample, **h** higher magnification of region 1 in **g**, **i** higher magnification of region 2 in **g**

in SMIT with respect to other processes such as SMAT, the effect of the ball size is not the same. In the SMIT, the balls do not fly in the chamber but just act as a medium to transfer the impact energy. Thus, with a smaller ball size and consequently a much higher number of impacts, more effective grain refinement with higher overall mechanical performance is achieved. The higher properties (such as microstrain, dislocation density, martensite fraction, and yield stress) in the case of the 3.5–2 sample could be justified with this rationale.

Regarding the microstructural features revealed by TEM and FESEM observations (Sect. 3.1) and XRD analysis (Sect. 3.2), various hardening mechanisms can be suggested to give a clear description of the nanocrystallization behavior (Figs. 13 and 14) and to compose some kind of a general expression describing the hardening process. First, the surface layer of the deformed stainless steel becomes very similar to a composite-like material. It includes the ε and α′martensite in an austenite matrix. The formation mechanism of refined microstructure in the superficial layer comprises a combined process of dislocation generation and interaction, deformation-induced martensitic transformation, and deformation twinning, identical to the processes identified in the similar material treated by SMAT [22].

Four main mechanisms can be suggested to explain the hardening behavior: (a) A decrease in grain/cell/twin spacing size, (b) deformation twins, (c) dislocation entanglements and sub-boundaries formation, and (d) martensite transformation. All the above-mentioned mechanisms play a role in the hardening process. As could be seen in Table 4, the grain size estimated by XRD analyses decreases from 50 μm to below 30 nm, in good agreement with the microstructure observed by TEM in the surface layer of the SMIT samples (Fig. 9c). The formation of nanosized grains in the AISI 316L sample during SMIT may have two paths: (i) fragmentation of nanotwin bundles and (ii) slip banding in nano twin bundles. As regards the former path, within the nanoscale twin/matrix lamellae, interconnecting boundaries are created by dislocation buildup and rearrangement, reordering the twin/matrix lamellae into refined blocks. The orientation of these refined blocks increases with the interaction of more dislocations with the interconnecting boundaries or twin boundaries. Eventually, the twin/matrix lamellae are fragmented into nanosized grains, of which the sizes are almost equivalent to the twin/matrix lamellar thickness. For the latter path, with increasing strains, deformation
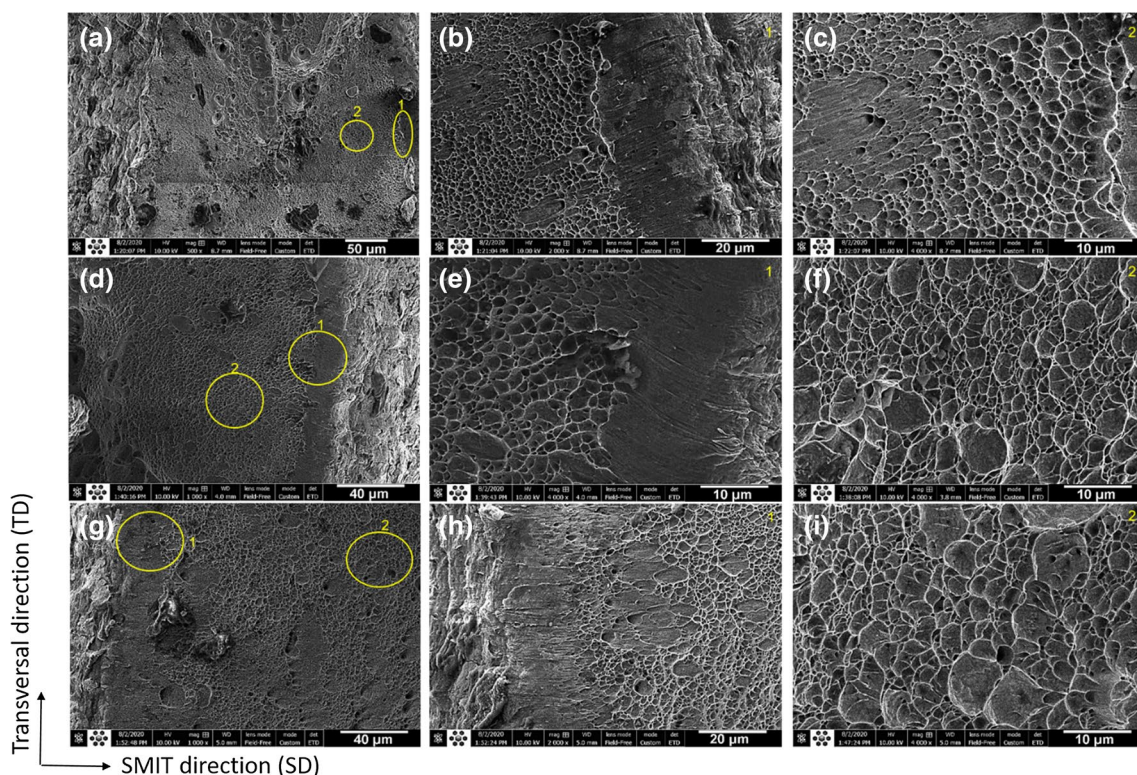
Fig. 16 Fracture surface morphology of **a** 5.0–0.5 sample, **b** region 1 in **a**, **c** region 2 in **a**, **d** sample 5.0–1, **e** region 1 in **d**, **f** region 2 in **d**, **g** 5.0–2 sample, **h** region 1 in **g**. **i** region 2 in **g**

twinning cannot sustain homogeneous plastic deformation and slip banding takes place and penetrates the twin/matrix lamellae due to stress localization, resulting in twisting and fragmentation of the twin/matrix lamellae. Consequently, nanosized grains with random orientations are formed within the bands. According to TEM observations (Fig. 7a–c) and FESEM images (Fig. 5), it can be suggested that the deformation twins and their intersections serve as nuclei for the martensite formation. Based on the XRD, dislocation density have a drastic increase from ~ 10^{10} m^{-2} in the untreated condition to 10^{14} m^{-2} in the SMITed sample. Martensite peaks can be observed in XRD patterns (Fig. 11). Generally, during deformation, austenitic stainless steels with SFE < 18 mJ m^{-2} transform into martensite, whereas dislocation activities become more dominant when SFE > 45 mJ m^{-2} [63]. The calculated SFE values using XRD are not accurate enough and usually require modification factors. Thus, it is not convenient to discuss the formation of martensite based on the calculated SFE values. However, at the earliest stages of the deformation, twining is dominant as can be seen in Fig. 17. To examine the present phases in the treated samples, peak identification and indexing of XRD patterns were done (Fig. 11). Martensitic peaks can be observed in the topmost surface layer of deformed specimens, the

fraction of which is found to be considerable; also confirming the calculated SFE (0.2–3 mJ/m^2). Deformation conditions are suitable to produce martensite and have an impact on the strength and ductility of the treated material. This suggests that under SMIT conditions, there are phase transformations in AISI 316L stainless steel. The yield point for the SMIT sample 3.5–2 increases by 150% where its large volume fraction of martensite (Table 5) indicates a certain effect in the increments in both the yield strength and ultimate strength values.

Previous studies showed that during deformation in austenitic stainless steels, α′ martensite nucleated at the intersection of two ε martensite laths [64], and the SFs formed could be martensite embryos. Venables [65] found that the ε-phase can be an intermediate one in the nucleation of α′martensite from the austenitic matrix. In studies by Guo et al. [66] and Hsu and Zuyao [67], the γ → ε transformation mechanism is discussed. SFE or SFP plays a crucial role in the calculation of the critical driving force ΔG_γ for the martensitic transformation of FCC (γ) → HCP (ε).

The (1 1 0) $_{\alpha'}$ and (2 1 1) $_{\alpha'}$ reflections indicate the presence of α′ martensite. Using the (2 1 1) $_{\alpha'}$ reflection, the volume fraction of martensite ($f_{\alpha'}$) was estimated according to Eq. (6) [68]:
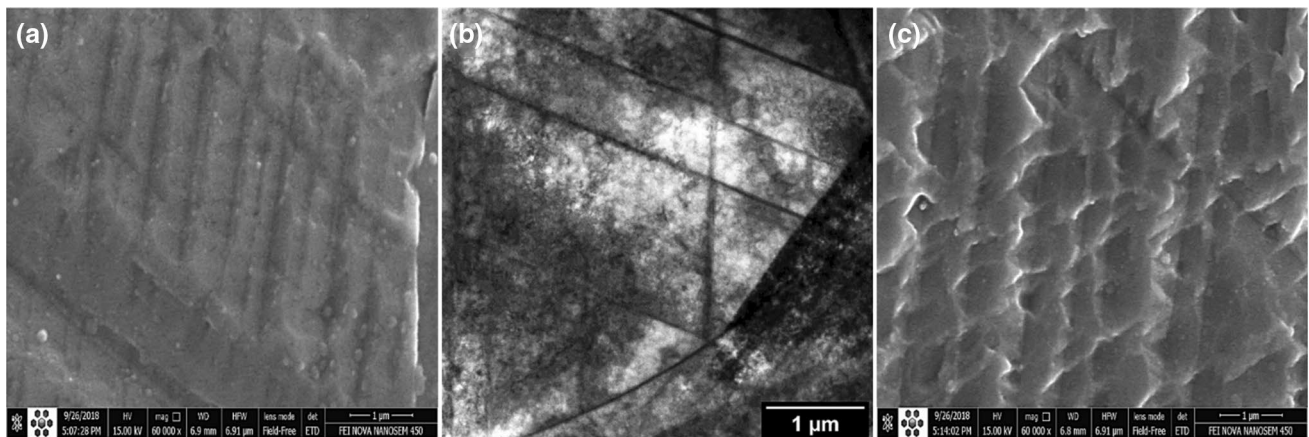
Fig. 17 **a** Deformation twins in SMITed sample for 30 min and 5 mm ball with FESEM observation, **b** TEM observation of twins and their intersections for 5.0–0.5 sample and **c** deformation twins in SMITed for 30 min and 3.5 mm ball

Table 5 Calculated volume fraction of α′ martensite (f$_{α'}$) for SMITed samples

sample	Volume fraction of α′ martensite (f$_{α'}$), %
5.0–0.5	-
5.0–1	19
5.0–2	25
3.5–0.5	-
3.5–1	20
3.5–2	42

$$f_{α'} = 1 - \frac{0.65(I_{311γ} + I_{220γ})}{I_{211α'} + 0.65(I_{311γ} + I_{220γ})} \qquad (6)$$

Using Eq. (6), the volume fraction of α′ martensite was calculated for each sample. The volume fraction of martensite is shown in Table 5 for the samples treated for 1 h and 2 h. It is observed that regardless of the ball size, the martensite fraction increases with increasing SMIT time. At longer SMIT times, a greater accumulated strain extent results in higher f$_{α'}$ and thus larger diffraction peaks of the α′ martensite. This is consistent with the outcomes of the other SPD processes like laser shot peening [69], high energy shot peening [70] and vacuum-UIT [71, 72] where f$_{α'}$ was reported to increase as the processing time (strain extent) increased.

As can be seen, an increase in the treatment time results in an increase in the fraction of α′ martensite. In a recent study [73], the dependence of austenite grain size on γ → α′ transformation was shown in which the amount of α′ martensite increases by decreasing austenite grain size.

The interaction process between dislocations and large SFTs is observed in Fig. 18 and Fig. 19. Experimental studies of the interaction between dislocations and SFTs have shown that there are three common interactions: replacement of the tetrahedron with a Frank loop; absorption of the tetrahedron into the dislocation, which leaves no residual defect; and replacement of the original tetrahedron with a smaller one, which corresponds to the apex of the original tetrahedron [74–77]. The tetrahedron is a strong barrier to dislocation motion. Various interactions were observed, including shearing of the tetrahedron followed by slip bands or deformation twinning which leaves behind a complex irreversible defect (Fig. 18a) and a smaller tetrahedron (Fig. 18b–d). The intersection of the slip plane with the face of the tetrahedron resulted, at least, in partial annihilation of the tetrahedron or its replacement with another type of defect (Fig. 18e, f).

The strengthening effect of SFTs with a size of ∼30 nm–3 μm in SMIT samples is important; it is believed that SFTs are effective in blocking dislocation motion [78].

The images presented in Fig. 19 show the interactions of dislocation as it moves through a field of tetrahedra in an SMIT sample (5.0–0.5). It can be seen that the intersection of the dislocation with the edge of the tetrahedron leads to dislocation cross-slip, neither with any obvious interaction nor any effect on the tetrahedron.

5 Conclusions

The surface nanocrystallization behavior of AISI 316L stainless steel was investigated using Surface Mechanical Impact Treatment (SMIT). The mechanical performance was

Fig. 18 **a** Shearing of the SFT followed by slip bands or deformation twins in 5.0–1 sample, **b** higher magnification of smaller SFT generated from the shearing of a tetrahedron in 5.0–1 sample, **c** SFT and their interaction with slip bands in 3.5–1 sample, **d** higher magnification of selected areas in **c**, **e** intersection of the slip plane with the face of the SFT in 5.0–2 sample, **f** higher magnification of partial annihilation of the SFT in 5.0–2 sample
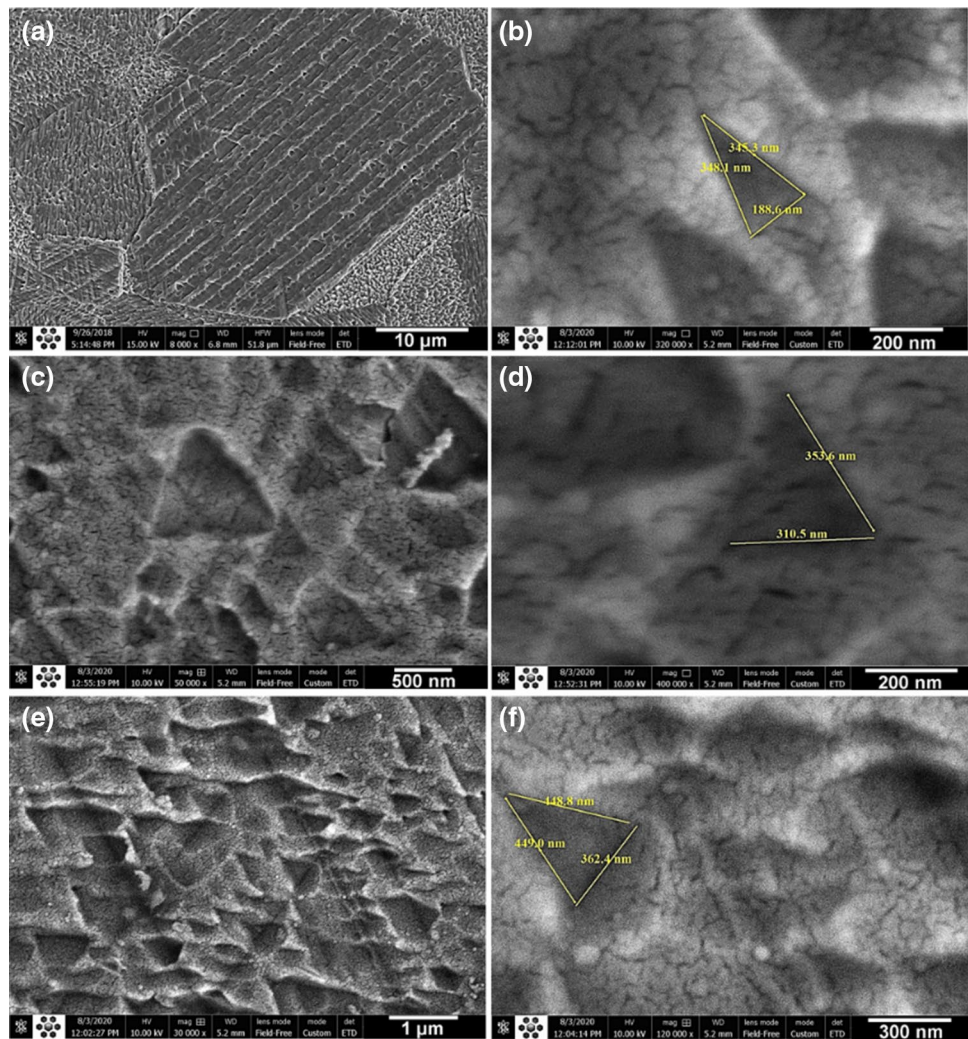
studied using microhardness and tensile testing. The following conclusions were drawn:

- Various microstructures with a characteristic gradient behavior, from martensite to twins, dislocation tangles, and slip bands were formed through the deformed surface layer. The average grain size of the final structure in the topmost treated surfaces was successfully refined to ~20 nm. The dislocation content was increased significantly (~10^{14} m^{-2}) compared to the untreated sample (10^{10} m^{-2}).
- Slip bands and nanotwining was detected to be the most probable mechanism for the grain refinement and nanocrystallization process.
- Martensitic phase transformation was induced during the treatment due to the high strain rate severe plastic deformation. The volume fraction of martensite was

estimated to be ~19%–42% depending on SMIT processing conditions.
- The surface layer of the treated stainless steel became very similar to a composite-like material in which twining, slip bands, and deformation-induced α′ and ε martensite were formed. The dominant deformation mechanism changed from twining to martensitic phase transformation with increasing SMIT time as well as accumulated strain.
- The nanostructured steel samples exhibited a 2.5-time increase in the tensile strength and around a 3-time increase in microhardness hardness at the treated surface, proving the overall enhancement in the structural integrity upon using SMIT.
- Stacking-fault tetrahedrons (SFT) were formed during SMIT with a size of 30 nm–3 μm. This seems to be a capability of the SMIT since the previously investigated surface SPD methods did not report SFT observation.

Fig. 19 Series of images of different areas at the 5.0–0.5 sample showing the interaction of the dislocation with SFT. White arrows indicate SFT and black arrows indicate dislocation
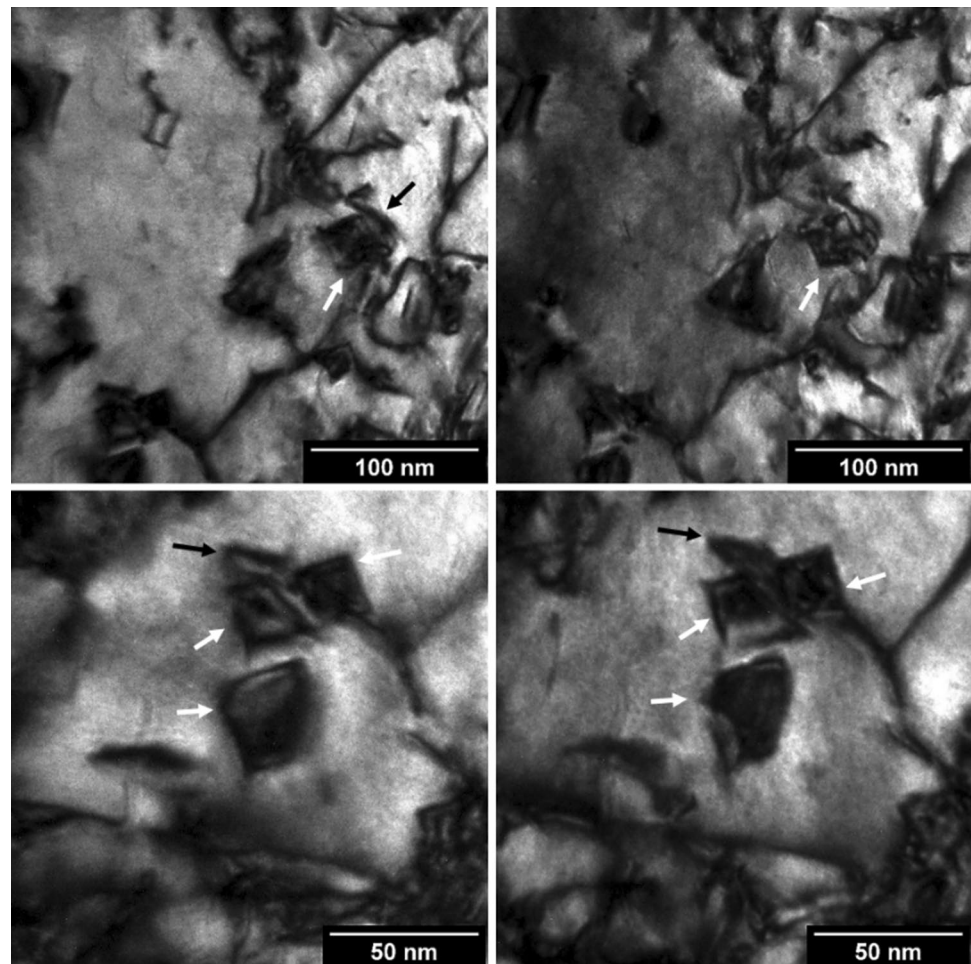
SFT formation can be justified by the higher imposed strain in the SMIT technique. TEM and FESEM analyses suggested that the formation of SFT is based on the dislocation mechanism.

Declaration

Conflict of Interest On behalf of all authors, the corresponding author states that there is no conflict of interest.

References

1. K.S. Kumar, H. Van Swygenhoven, S. Suresh, Acta Mater. **51**, 5743–5774 (2003). https://doi.org/10.1016/j.actamat.2003.08.032
2. M.A. Meyers, A. Mishra, D.J. Benson, Prog. Mater. Sci. **51**, 427–556 (2006). https://doi.org/10.1016/j.pmatsci.2005.08.003
3. N.A. Dan Liu, D. Liu, X. Zhang, C. Liu, Mater. Sci. Eng. A **726**, 69–81 (2018). https://doi.org/10.1016/j.msea.2018.04.033
4. A.M. Hodge, Y.M. Wang, T.W. Barbee Jr., Mater. Sci. Eng. A **429**, 272–276 (2006). https://doi.org/10.1016/j.msea.2006.05.109
5. A. Zaffora, F. Di Franco, M. Santamaria, Curr. Opin. Electrochem. **29**, 100760 (2021). https://doi.org/10.1016/j.coelec.2021.100760
6. L. Ceschini, C. Chiavari, E. Lanzoni, C. Martini, Mater. Design **38**, 154–160 (2012). https://doi.org/10.1016/j.matdes.2012.02.019
7. S. Bagherifard, S. Slawik, I. Fernández-pariente, C. Pauly, F. Mücklich, M. Guagliano, Mater. Design **102**, 68–77 (2016). https://doi.org/10.1016/j.matdes.2016.03.162
8. Y.G. Liu, M.Q. Li, H.J. Liu, Mater. Charact. **123**, 83–90 (2017). https://doi.org/10.1016/j.matchar.2016.11.020
9. C.S. Montross, T. Wei, L. Ye, G. Clark, Y.-W. Mai, Int. J. Fatigue **24**, 1021–1036 (2002). https://doi.org/10.1016/S0142-1123(02)00022-1
10. S. Kalainathan, S. Sathyajith, S. Swaroop, Opt. Laser. Eng. **50**, 1740–1745 (2012). https://doi.org/10.1016/j.optlaseng.2012.07.007
11. S. Bahl, S. Suwas, T. Ungàr, K. Chatterjee, Acta Mater. **122**, 138–151 (2017). https://doi.org/10.1016/j.actamat.2016.09.041
12. A. Heydari, R. Miresmaeili, S. Bagherifard, M. Guagliano, M. Aliofkhazraei, Mater. Design **116**, 365–373 (2017). https://doi.org/10.1016/j.matdes.2016.12.045
13. T.O. Olumide, J. Lu, Nano Mater. Sci. **2**, 3 (2020). https://doi.org/10.1016/j.nanoms.2020.04.002

14. W.L. Li, N.R. Tao, K. Lu, Scripta Mater. **59**, 546–549 (2008). https://doi.org/10.1016/j.scriptamat.2008.05.003

15. Y.Z. Zhang, J.J. Wang, N.R. Tao, J. Mater. Sci. Technol. **36**, 65 (2019). https://doi.org/10.1016/j.jmst.2019.02.008

16. H.W. Huang, Z.B. Wang, J. Lu, K. Lu, Acta Mater. **87**, 150–160 (2015). https://doi.org/10.1016/j.actamat.2014.12.057

17. Y. Ye, S.-Z. Kure-Chu, Z. Sun, X. Li, H. Wang, G. Tang, Mater. Design **149**, 214–227 (2018). https://doi.org/10.1016/j.matdes.2018.04.027

18. M. Jamalian, D.P. Field, J. Mater. Sci. Technol. **36**, 45–49 (2020). https://doi.org/10.1016/j.jmst.2019.06.013

19. M. Dehghan, R. Miresmaeili, M. Askari-Paykani, H.R. Shahverdi, Met. Mater. Int. **28**, 1232–1245 (2022). https://doi.org/10.1007/s12540-021-01007-5

20. T. Roland, D. Retraint, K. Lu, J. Lu, Scripta Mater. **54**, 1949–1954 (2006). https://doi.org/10.1016/j.scriptamat.2006.01.049

21. F.K. Yan, G.Z. Liu, N.R. Tao, K. Lu, Acta Mater. **60**, 1059–1071 (2012). https://doi.org/10.1016/j.actamat.2011.11.009

22. R. Peng, L. Fu, L. Zhou, Appl. Surf. Sci. **388**, 406–411 (2016). https://doi.org/10.1016/j.apsusc.2015.12.103

23. Z.D. Wang, G.F. Sun, Y. Lu, M.Z. Chen, K.D. Bi, Z.H. Ni, Surf. Coat. Tech. **385**, 125403 (2020). https://doi.org/10.1016/j.surfcoat.2020.125403

24. S.M. Hassani-gangaraj, K.S. Cho, H.L. Voigt, M. Guagliano, C.A. Schuh, Acta Mater. **97**, 105–115 (2015). https://doi.org/10.1016/j.actamat.2015.06.054

25. Y. Liu, M. Li, Mater. Sci. Eng. A **669**, 7–13 (2016). https://doi.org/10.1016/j.msea.2016.05.088

26. R. Madhavan, S. Suwas, Acta Mater. **121**, 46–58 (2016). https://doi.org/10.1016/j.actamat.2016.08.036

27. W.H.S. Lou, Y. Li, L. Zhou, X. Nie, G. He, Y. Li, L. Yuqin, H. Weifeng, Mater. Design **104**, 320–326 (2016). https://doi.org/10.1016/j.matdes.2016.05.028

28. S.M. Dasharath, S. Mula, Mater. Design **99**, 552-564 (2016). https://doi.org/10.1016/j.matdes.2016.03.095

29. W.S. Zhao, N.R. Tao, J.Y. Guo, Q.H. Lu, K. Lu, Scripta Mater. **53**, 745–749 (2005). https://doi.org/10.1016/j.scriptamat.2005.05.022

30. S. Scheriau, Z. Zhang, S. Kleber, R. Pippan, Mater. Sci. Eng. A **528**, 2776–2786 (2011). https://doi.org/10.1016/j.msea.2010.12.023

31. M. Jayalakshmi, P. Huilgol, B. Ramachandra, K.U. Bhat, Surf. Coat. Tech. **344**, 295–302 (2018). https://doi.org/10.1016/j.surfcoat.2018.03.028

32. B. Schuh, R. Pippan, A. Hohenwarter, Mater. Sci. Eng. A **748**, 379–385 (2019). https://doi.org/10.1016/j.msea.2019.01.073

33. H.Q. Sun, Y.-N. Shi, M.-X. Zhang, K. Lu, Acta Mater. **55**, 975–982 (2007). https://doi.org/10.1016/j.actamat.2006.09.018

34. A.K. Agrawal, A. Singh, A. Vivek, S. Hansen, G. Daehn, Mater. Lett. **22**, 50-53 (2018). https://doi.org/10.1016/j.matlet.2018.04.044

35. R.D.K. Misra, V.S.A. Challa, P.K.C. Venkatsurya, Y.F. Shen, M.C. Somani, L.P. Karjalainen, Acta Mater. **84**, 339–348 (2015). https://doi.org/10.1016/j.actamat.2014.10.038

36. S.J. Wang, T. Jozaghi, I. Karaman, R. Arroyave, Y.I. Chumlyakov, Mater. Sci. Eng. A **694**, 121-131 (2017). https://doi.org/10.1016/j.msea.2017.03.073

37. Z. Fan, H. Xu, D. Li, L. Zhang, L. Liao, Procedia Eng. **27**, 1718–1722 (2012). https://doi.org/10.1016/j.proeng.2011.12.641

38. E. Maleki, N. Maleki, A. Fattahi, O. Unal, M. Guagliano, S. Bagherifard, Surf. Coat. Tech. **405**, 126729 (2021). https://doi.org/10.1016/j.surfcoat.2020.126729

39. G.K. Williamson, W.H. Hall, Acta Metall. **1**, 22–31 (1953). https://doi.org/10.1016/0001-6160(53)90006-6

40. R.E. Schramm, R.P. Reed, Metall. Trans. A **6**, 1345–1351 (1975)

41. J.-E. Jin, Y.-K. Lee, Acta Mater. **60**, 1680–1688 (2012). https://doi.org/10.1016/j.actamat.2011.12.004

42. J. Talonen, H. Hänninen, Acta Mater. **55**, 6108–6118 (2007). https://doi.org/10.1016/j.actamat.2007.07.015

43. K. Kumar, A. Pooleery, K. Madhusoodanan, R.N. Singh, J.K. Chakravartty, B.K. Dutta, R.K. Sinha, Procedia Engineer. **86**, 899–909 (2014). https://doi.org/10.1016/j.proeng.2014.11.112

44. J.W. Wang, S. Narayanan, J. Yu Huang, Z. Zhang, T. Zhu, S.X. Mao, Nat. Commun. **4**, 2340 (2013). https://doi.org/10.1038/ncomms3340

45. M.H. Loretto, P.J. Phillips, M.J. Mills, Scripta Mater. **94**, 1–4 (2015). https://doi.org/10.1016/j.scriptamat.2014.07.020

46. B.N Singh, N.M Ghoniem, H Trinkaus, J. Nucl. Mater. **307–311**, 159–170 (2002). https://doi.org/10.1016/S0022-3115(02)01095-4

47. R. Schäublin, Z. Yao, N. Baluc, M. Victoria, Philos. Mag. **85**, 769-777 (2005). https://doi.org/10.1080/14786430412331319929

48. J. Silcox, P.B. Hirsch, Philos. Mag. A **4**, 72-89 (1959). https://doi.org/10.1080/14786435908238228

49. H. Wang, D.S. Xu, R. Yang, P. Veyssie, Acta Mater. **59**, 19–29 (2011). https://doi.org/10.1016/j.actamat.2010.07.045

50. M.H. Loretto, A. Pavey, Philos. Mag. A **17**, 553-559 (1968). https://doi.org/10.1080/14786436808217742

51. Q. Wang, Q. Bai, J. Chen, Y. Guo, W. Xie, Appl. Surf. Sci. **355**, 1153–1160 (2015). https://doi.org/10.1016/j.apsusc.2015.06.176

52. M. Moallemi, A. Kermanpur, A. Naja, A. Rezaee, H.S. Baghbadorani, P.D. Nezhadfar, Mater. Sci. Eng. A **653**, 147–152 (2016). https://doi.org/10.1016/j.msea.2015.12.006

53. S. Vercammen, B. Blanpain, Acta Mater. **52**, 2005–2012 (2012). https://doi.org/10.1016/j.actamat.2003.12.040

54. D. Canadinc, H. Sehitoglu, H.J. Maier, Y.I. Chumlyakov, Acta Mater. **53**, 1831–1842 (2005). https://doi.org/10.1016/j.actamat.2004.12.033

55. H.J. Bae, K.K. Ko, M. Ishtiaq, J.G. Kim, H. Sung, J.B. Seol, J. Mater. Sci. Technol. **115**, 177–188 (2022). https://doi.org/10.1016/j.jmst.2021.11.027

56. M.A. Vasylyev, B.N. Mordyuk, S.I. Sidorenko, S.M. Voloshko, A.P. Burmak, Surf. Coat. Tech. **343**, 57–68 (2018). https://doi.org/10.1016/j.surfcoat.2017.11.019

57. V. Azar, B. Hashemi, M.R. Yazdi, Surf. Coat. Tech. **204**, 3546–3551 (2010). https://doi.org/10.1016/j.surfcoat.2010.04.015

58. P. Peyre, X. Scherpereel, L. Berthe, C. Carboni, R. Fabbro, G. Béranger, C. Lemaitre, Mater. Sci. Eng. A **280**, 294–302 (2000). https://doi.org/10.1016/S0921-5093(99)00698-X

59. X.H. Chen, J. Lu, L. Lu, K. Lu, Scripta Mater. **52**, 1039–1044 (2005). https://doi.org/10.1016/j.scriptamat.2005.01.023

60. K. Lu, J. Lu, Mater. Sci. Eng. A **357-377**, 38–45 (2004). https://doi.org/10.1016/j.msea.2003.10.261

61. P. Zhang, J. Lindemann, Scripta Mater. **52**, 485–490 (2005). https://doi.org/10.1016/j.scriptamat.2004.11.003

62. S. Bagherifard, I.F. Pariente, R. Ghelichi, M. Guagliano, Procedia Eng. **2**, 1683–1690 (2010). https://doi.org/10.1016/j.proeng.2010.03.181

63. Y.F. Shen, X.X. Li, X. Sun, Y.D. Wang, L. Zuo, Mater. Sci. Eng. A **552**, 514–522 (2012). https://doi.org/10.1016/j.msea.2012.05.080

64. K. Datta, R. Delhez, P.M. Bronsveld, J. Beyer, H.J.M. Geijselaers, J. Post, Acta Mater. **57**, 3321–3326 (2009). https://doi.org/10.1016/j.actamat.2009.03.039

65. J.A. Venables, Philos. Mag. A **7**, 35–44 (1962). https://doi.org/10.1080/14786436208201856

66. Z. Guo, Y. Rong, S. Chen, T.Y. Hsu, Scripta Mater. **41**, 153–158 (1999). https://doi.org/10.1016/S1359-6462(99)00134-7

67. T.Y. Hsu, X. Zuyao, Mater. Sci. Eng. A **273-275**, 494–497 (1999). https://doi.org/10.1016/S0921-5093(99)00386-X

68. A. Etienne, B. Radiguet, C. Genevois, J.-M. Le Breton, R. Valiev, P. Pareige, Mater. Sci. Eng. A **527**, 5805–5810 (2010). https://doi.org/10.1016/j.msea.2010.05.049

69. C. Ye, S. Suslov, D. Lin, G.J. Cheng, Philos. Mag. **92**, 1369-1389 (2012). doi:https://doi.org/10.1080/14786435.2011.645899.

70. K.P. Staudhammer, L.E. Murr, S.S. Hecker, Acta Mater. **31**, 267–274 (1983). https://doi.org/10.1016/0001-6160(83)90103-7

71. B.N. Mordyuk, Y.V. Milman, M.O. Ie, G.I. Prokopenko, V.V. Silberschmidt, M.I. Danylenko, A.V. Kotko, Surf. Coat. Tech. **202**, 4875–4883 (2008). https://doi.org/10.1016/j.surfcoat.2008.04.080

72. B.N. Mordyuk, G.I. Prokopenko, M.A. Vasylyev, M.O. Iefimov, Mater. Sci. Eng. A **458**, 253–261 (2007). https://doi.org/10.1016/j.msea.2006.12.049

73. Y.F. Shen, N. Jia, Y.D. Wang, X. Sun, L. Zuo, D. Raabe, Acta Mater. **97**, 305–315 (2015). https://doi.org/10.1016/j.actamat.2015.06.053

74. Y. Matsukawa, Y.N. Osetsky, R.E. Stoller, S.J. Zinkle, Philos. Mag. **88**, 581-597 (2008). https://doi.org/10.1080/14786430801898644

75. Y. Matsukawa, Y.N. Osetsky, R.E. Stoller, S.J. Zinkle, J. Nucl. Mater. **351**, 285–294 (2006). https://doi.org/10.1016/j.jnucmat.2006.02.003

76. J.S. Robach, I.M. Robertson, H.-J. Lee, B.D. Wirth, Acta Mater. **54**, 1679–1690 (2006). https://doi.org/10.1016/j.actamat.2005.11.038

77. Y. Matsukawa, S.J. Zinkle, J. Nucl. Mater. **329-333**, 919–923 (2004). https://doi.org/10.1016/j.jnucmat.2004.04.069

78. M. Briceño, J. Kacher, I.M. Robertson, J. Nucl. Mater. **433**, 390–396 (2013). https://doi.org/10.1016/j.jnucmat.2012.10.004